



Progress in the development of a versatile table-top kHz-rate laser-plasma accelerator for mixed radiation sources

ANIL K. PATNAIK,^{1,*} MICHAEL L. DEXTER,¹ KYLE D. FRISCHE,¹ BENJAMIN M. KNIGHT,¹ NATHANIEL TAMMINGA,² RONAK DESAI,² JOSEPH SNYDER,³ CHRIS M. ORBAN,² AND ENAM A. CHOWDHURY^{2,4}

¹Department of Engineering Physics, U.S. Air Force Institute of Technology, Wright-Patterson AFB, Ohio 45433, USA

²Department of Physics, The Ohio State University, Columbus, Ohio 43210, USA

³Department of Mathematical and Physical Sciences, Miami University, Hamilton, Ohio 45056, USA

⁴Department of Materials Science and Engineering, The Ohio State University, Columbus, Ohio 43210, USA

*anil.patnaik.2@us.af.mil

Received 3 February 2025; revised 22 April 2025; accepted 25 April 2025; posted 28 April 2025; published 2 June 2025

Ultra-intense laser and plasma interactions with their ability to accelerate particles reaching relativistic speed are exciting from a fundamental high-field physics perspective. Such relativistic laser-plasma interaction (RLPI) offers a plethora of critical applications for energy, space, and defense enterprise. At AFIT's Extreme Light Laboratory (ELL), we have demonstrated such RLPI employing a table-top ~ 10 mJ, 40 fs laser pulses at a kHz repetition rate that produce different types of secondary radiations via target normal sheath acceleration (TNSA). With our recent demonstration of laser-driven fusion, the secondary radiations generated are neutrons, x-ray emission, and MeV energy electrons and protons—all at a kHz rate. To achieve the high repetition rate, we developed the enabling kHz-repetition-rate-compatible liquid targets in the form of microjets, droplets, and submicron-thick sheets. These targets, combined with high repetition rate diagnostics, enable a unique, real-time feedback loop between the experimental inputs (laser and target parameters) and generated sources (x-rays, electrons, ions, etc.) to develop machine learning (ML)-based control of mixed radiation. The goal of this paper is to provide an overview of the capabilities of ELL, describe the diagnostics and characteristics of the secondary radiation, data analysis, and quasi-real-time ML functionality of this platform that have been developed over the last decade and a half.

© 2025 Optica Publishing Group. All rights, including for text and data mining (TDM), Artificial Intelligence (AI) training, and similar technologies, are reserved.

<https://doi.org/10.1364/AO.558553>

1. INTRODUCTION

As highlighted in the recent multi-agency report [1], the world is entering an exciting era of high average power ultra-intense lasers, where these lasers can open pathways to study not only fundamental quantum relativistic high field science [2], but also numerous cutting-edge applications like laser proton therapy [3], or develop next-generation tools like laser-based compact particle accelerators for electrons [4] or ions [5] or TeV colliders [6,7]. Most of these future needs require high repetition rate (\geq kHz) operation, which necessitates a precision laser target system [8,9] that can operate in a relativistic intensity regime with kHz or higher repetition rate. Whereas most ultra-intense laser systems operate in single-shot mode or with a rate approaching 1 Hz [10], at the “Extreme Light Laser” (ELL) Laboratory based at the Air Force Institute of Technology (AFIT) located inside Wright-Patterson Air Force

Base (WPAFB), Ohio, we created a unique high repetition rate relativistic laser-plasma interaction (RLPI) system with a unique liquid target capability that replenishes every millisecond to offer a new target to the incoming kHz-rate laser pulse [11]. Cutting-edge research has been conducted with this RLPI system for over a decade [11–18]. From its inception, the goal has been to establish table-top ultra-intense laser systems as a kind of all-in-one source of unique secondary radiation to meet defense and space industry needs and applications. A diagram representing the energies and generation rate of different radiation sources is depicted in Fig. 1. Although the repetition rates of ultra-intense laser systems around the world are increasing [19,20], high-repetition-rate diagnostics of secondary radiation in ultra-intense laser experiments remain an important challenge in the RLPI field [21]. We outline our efforts and progresses made in the last decade and a half to address these challenges throughout this paper.

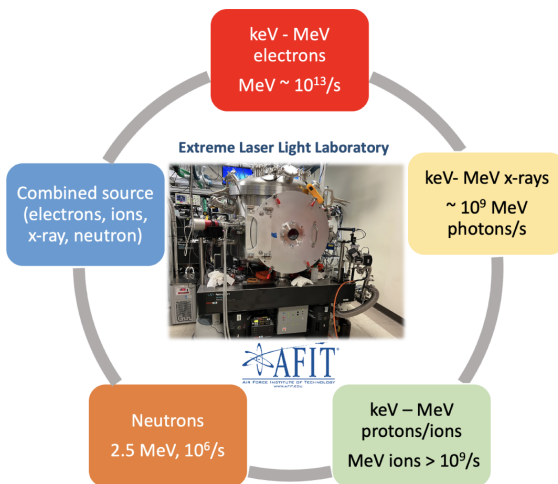


Fig. 1. Energy and generation rate of ELL's secondary radiation demonstrations, and the ability to generate mixed radiation at kHz rate.

Recently, we have ramped up work on developing a turn-key solution for a small, fast neutron source using a liquid target-RLPI at a high repetition (kHz) rate. Our laser-driven fusion system produces monoenergetic neutrons in distinctly timed packets a thousand times a second (about 10^2 – 10^3 neutrons/shot, i.e., 10^5 – 10^6 neutrons/s), allowing for high-fidelity time-of-flight characterization with a low-noise background [18]. By choosing the appropriate target material, the system is tunable over a wide range of neutron energies with very narrow energy peaks. Additional investment can lead to much higher neutron fluxes in the future (10^{13} – 10^{14} neutrons/s, well beyond what is possible with commercially available DD generators) as well as the possibility of DT fusion (resulting in higher energy neutrons and even higher fluxes). The ELL will look to rapidly advance this unique neutron production capability toward producing viable nuclear data measurements for a minor enduring investment while working on optimizing the source using a machine learning (ML) algorithm.

The paper is organized as following: in Section 2, we describe the details of the ultra-intense laser system, and the controls and characteristics of the laser pulses produced. In Section 3, we discuss the details of our flowing liquid target system. In Section 4, we describe the suite of diagnostics used in the experiment. In Section 5, we describe the close-loop computer systems that control the laser and describe current capabilities for quasi-real-time ML in order to optimize and control the secondary radiation produced. In Section 6, we summarize the capabilities and discuss the outlook.

2. LASER ARCHITECTURE: CONTROLS AND CHARACTERISTICS

The laser system was designed and constructed with several goals in mind, first, to achieve peak intensities above the relativistic interaction threshold of 10^{18} Wcm $^{-2}$; second, the laser has to be robust enough to survive 1 kHz repetition rate extreme laser plasma interaction, where a strong back-reflection can destroy optical components in nanoseconds; third, the laser

system needs precise pre-pulse control, i.e., extremely high pre-pulse contrast in the main laser line along with the capability to introduce a pre-pulse with varying energy at a specific temporal delay; and fourth, the system needs a dynamic visual probing system to capture relativistic laser plasma dynamics with high spatiotemporal resolution over many orders of magnitude in time. Our unique system striving toward achieving all the goals is described in detail below.

A picture of the ELL and the laser layout with control and detection, and the target chamber is presented in Fig. 2. The laser system consists of dual chirped pulse amplification (DCPA), which is a popular architecture to create a high-repetition-rate reliable laser system to achieve the above goals. Our DCPA Ti:sapphire system was constructed to operate at a 780 nm center wavelength with a kHz repetition rate. A Ti:sapphire oscillator (KML Griffin-V) creates the seed pulses with a 70+ nm bandwidth at a repetition rate of $80,000,500 \pm 8$ Hz. These pulses are temporally stretched using a reflection grating-based pulse stretcher (1200 li/mm grating) to 150 ps. The pulses are then sent into a cryo-cooled modified KMLabs multipass amplifier, which produces 2.0 mJ/pulse after pulse cleaning using a Pockel cell and high-contrast polarizers at a reduced laser repetition rate of 1.0 kHz. Then the pulses are sent to a grating compressor after beam expansion with a reflective telescope. The output from the compressor resulted in 1 mJ/pulse energy compressed to a 35 fs pulse duration. The pulses are then spatially filtered and sent to a cross-polarization wave (XPW) filter setup [22], where two z-cut BaF₂ crystals were used as polarization rotation nonlinear media between two high-contrast α -BBO Glan polarizers (pre-pulse to main pulse contrast $\sim 10^{-6}$:1) in a null setup (90 deg rotated). This way, only the highest-intensity portion of the ultrashort pulse, rotated 90 deg by cross-polarization wave generation, can exit the setup, rejecting noise pre- and post-pulse. With 60 μ J input, we were able to extract 10 μ J. The XPW operation enhanced the pulse contrast by $\sim 10^5$ while enabling significant nonlinear frequency broadening and mode cleaning (see Fig. 3). The cleaned pulses were then sent to a pulse stretcher, which utilizes a cylindrical reflector, high-efficiency transmission grating (Lightsmyth) at 1400 li/mm. Then the pulses enter into a five-pass Brewster's cut Ti:Sapphire cryo-cooled custom-designed high-power multipass amplifier, where the crystal is pumped with 35–40 mJ/pulse from each side, using two photonics industries' pump lasers, producing an amplified output of 22 mJ/pulse from a typical 10 μ J input. The kHz repetition rate pulses then enter a dual thin film polarizer (TFP) and large aperture Pockel's cell setup (TFP1 at the entrance and TFP2 at the exit), where the nanosecond pulse contrast is enhanced, and potential back reflection is prevented from propagating onto the amplifier by electro-optic gating.

Thereafter, the laser pulses enter a dual-transmissive-grating compressor (Lightsmyth 1400 li/mm transmission gratings), which compresses the pulses to 30 fs, with an output pulse energy of 11 mJ. After compression, a small portion of the pulses is picked off to generate a controlled pre-pulse, with temporal delay and energy control via motorized translation stages and waveplate thin film polarizer combination. The pre-pulse and the main pulse then travel collinearly to the experimental chamber. This design offers pre-pulse a maximum energy of 10 μ J

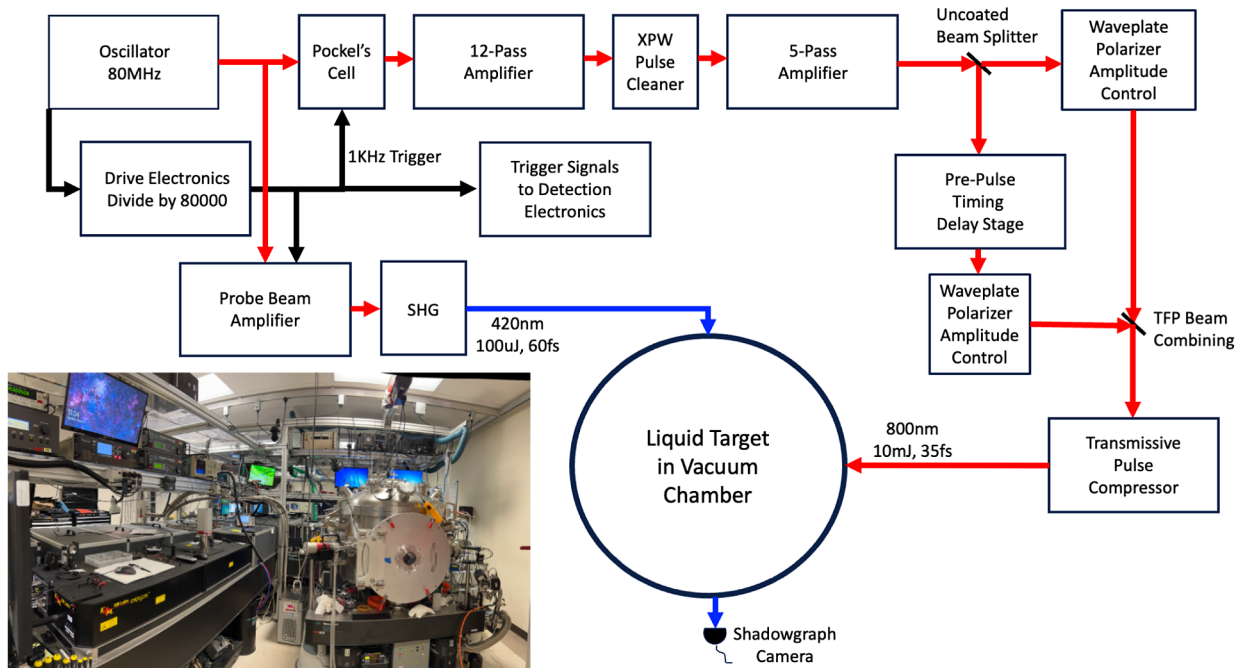


Fig. 2. Layout of the 35 fs, 10 kHz, 10 mJ laser, the liquid target chamber, and the 50 fs resolution shadography camera. The inset is a picture of the ELL Laboratory.

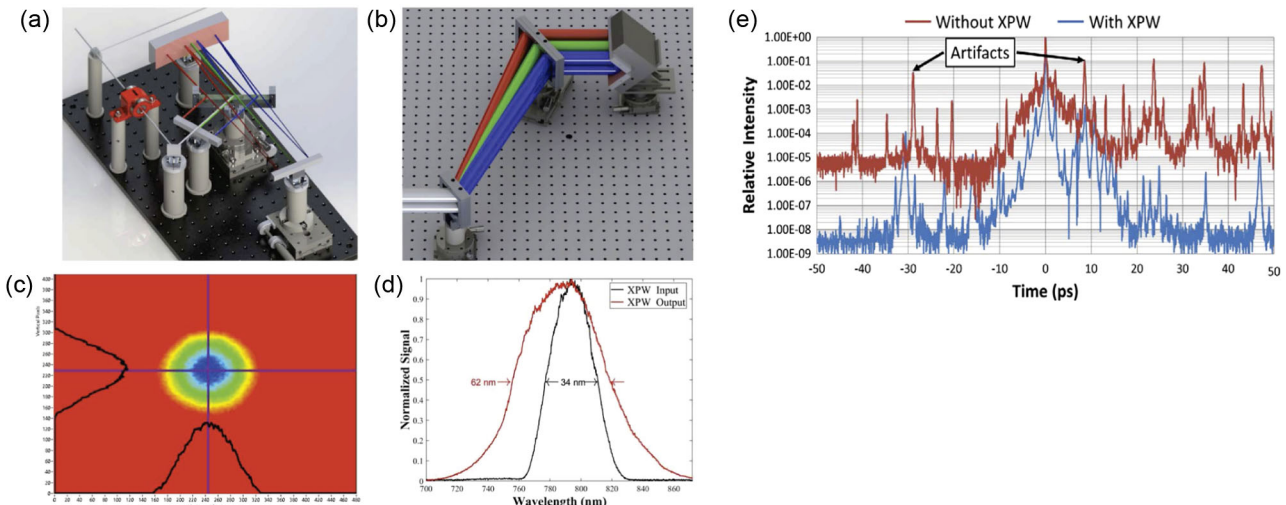


Fig. 3. Beam control architecture: (a) the pulse stretcher, (b) compressor, (c) the beam trace, (d) the XPW input and output, (e) 4–5 orders of magnitude suppression of the pedestal of the main pulse using XPW. Note that the “pre-pulse” appearing at $t = -32$ ps is an artifact of the “with XPW” blue trace measurement, corresponding to the $t = -28$ ps artifact present and identified for the “without XPW” red trace.

and a maximum delay of -160 ps with respect to the peak of the main pulse.

A. Shadography Probe with 50–80 fs Resolution

For the spatiotemporal study of the RLPI, we have developed a unique frequency-shifted shadowgraphic probe system capable of capturing the images of the interactions with a temporal resolution of 50–80 fs and a spatial resolution of 1 μm . The probe line is generated via a separate Ti:sapphire amplifier system (Coherent Legend) that is seeded by a pickoff from

the master oscillator so that the two systems are optically synchronized. The oscillator spectra are broadened and passed through a frequency filter before seeding into the amplifier to shift the amplified and compressed pulse spectrum to a center wavelength of 840 nm, with a 80 fs pulse duration. The pulses are then frequency-doubled in a nonlinear crystal to provide a 420 nm probe for the system, which can be separated from the plasma self-emission and coherent transition radiation emission from RLPI centered at 390 nm using a notch filter. The ultrahigh-intensity pump and the 420 nm probe cross each other orthogonally at the interaction region (see Fig. 2).

After the probe passes the interaction region, it is imaged onto a CCD using a high-resolution microscope objective (Mitutoyo, 10 \times or 20 \times for maximum resolution). This process enables us to capture high-fidelity, background plasma-noise-free spatiotemporally resolved images of the RLPI with liquid targets in transmission mode.

The specific timing and the delay of the probe pulse with respect to the pump pulse are controlled seamlessly via a combination of an electronic clock and a motorized stage providing a 13 ns optical delay. If a probe delay of +T nanoseconds is required, it is calculated via $T = N * 13 + \tau$, where N is a specific number of oscillator pulses skipped between seeding the pump or the probe amplifier system, and τ is the delay between 0 and 13 ns, created by the optical delay line (ultimate time resolution limited by the finest stage movement and the probe pulse duration), which cannot be achieved electronically. This way, we can achieve a $\pm 10 \mu\text{m}$ probe temporal delay with ≤ 80 fs resolution. The whole system is controlled via the Labview suite of codes, which allows capturing of RLPI transmission shadowgraphy movies with hundreds of frames with the click of a button (e.g., see supplementary info. at Ref. [16]). Note that the pump and probe are optically locked; hence, there is no timing jitter in the traditional sense from either of them. However, the timing delay error between the pump and probe comes from the variation in oscillator repetition rates. The timing error of the oscillator is one part in a million, e.g., the oscillator repetition frequency is $80,00,500 \pm 8$ Hz, which will translate to a 1 ps error for 1 μs delay for the pump and probe.

The 19 mm ($1/e^2$) diameter pump beam is focused onto the liquid target in the vacuum chamber with a custom precision-protected gold-coated f/1 off-axis parabola made out of fused silica (Aperture Optical Sciences), with a reflection focal distance of 30 mm. A typical pump focal spot size has 1.7 μm FWHM, enabling us to achieve peak intensities $\geq 10^{19} \text{ Wcm}^{-2}$.

3. LIQUID TARGET FOR HIGH-REPETITION-RATE RLPI

Our custom-designed liquid target system is described in detail in Ref. [11]. Here, we highlight some of the salient details. It should be noted that our liquid target system has been demonstrated to operate at the 1.0 kHz repetition rate of the laser system, whereas other schemes, like tape drives, to produce fresh targets with precision alignment, often cannot operate at such a high repetition rate [23–25]. Specifically, because while the liquid target system offers a very repeatable new target for the incoming kHz-rate laser pulse by replenishing within a millisecond, it is not as straightforward in the solid targets.

Furthermore, the liquid target system is capable of producing a variety of targets. A few representative targets generated at ELL are presented in Fig. 4. Most of the experiments performed to date use either a liquid cylindrical column (i.e., a rapidly flowing jet of liquid) or a thin liquid sheet formed from two liquid jets that are positioned so that the edges of the two jets are touching. Another common target geometry that is possible with our system is isolated droplets. Other target geometries are possible, and Ref. [11] includes a section on “exotic liquid targets.” For example, “isolated disk targets” are formed from the collision of two liquid droplets with a pancake-like appearance. Other interesting configurations include the liquid sheet’s surface tension producing a fluid “wire” generating a cone-wire target, which raises some interesting possibilities for creating large return currents and producing warm dense matter. The interested reader is referred to Ref. [11] for details.

The most common liquid target setup used in our experiments is the thin liquid sheet. In the literature, this setup is sometimes called a “liquid leaf” [26]. This configuration is the most often used because it produces the thinnest surface for the laser to interact with, and the maximum proton or deuteron energy from ultra-intense laser interactions is well-known to scale inversely with target thickness (e.g., Ref. [27]). We routinely produce liquid sheet targets of order 0.5 microns in thickness using our system. This advance helped us to achieve ≥ 2.5 MeV proton acceleration from only 3 mJ of laser energy on target, as described in Ref. [15], which was significantly higher than other groups that had achieved with similar laser energies and intensities. A shadowgraphic image sequence of the plasma with 50 fs progression is shown in Figs. 5(a), 5(b), 5(c), 5(d), 5(e), and 5(f), and an estimate of the relativistic expansion rate of the plasma (both measured and simulation) is presented in Fig. 5(g). Since that paper was published, other facilities have adopted similar schemes for producing targets from ion acceleration (e.g., Ref. [28]) to relativistic oscillating mirror (ROM) attosecond pulse generation with near single-cycle pulses [29].

Our custom liquid target system has been used with different liquids, including water, heavy water, and ethylene glycol. Experiments with deuterated ethylene glycol sheet target are in progress.

4. RADIATION GENERATION AND DIAGNOSTICS SUITE

To understand the RLPI-based radiations and measure the generated relativistic radiation at a high repetition rate, we have implemented a suite of detectors for each of the radiation (electron, proton, x-ray, and neutron), as depicted in Fig. 6. While electron and proton detectors operate inside the target chamber,

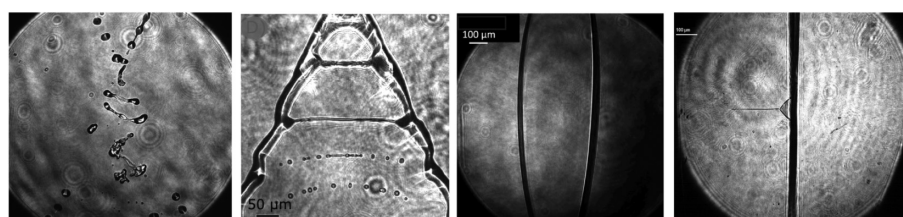


Fig. 4. Our ability to produce different target shapes at kHz rate. Shown here are [left to right] barbell, ladder, thin sheet, and cone-wire targets.

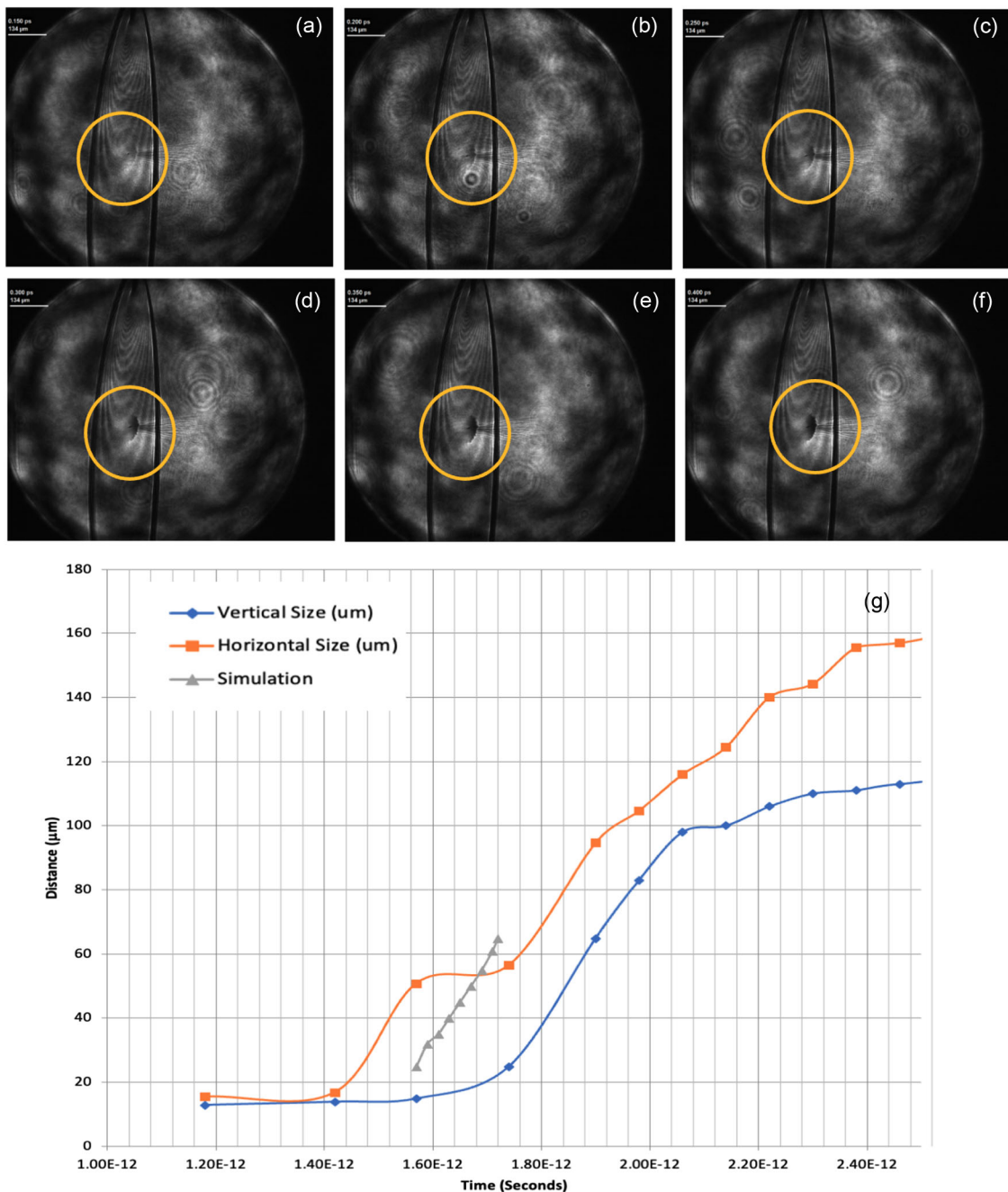


Fig. 5. The shadowgraphy images of the plasma evolution (a)–(f) between 150 and 400 fs after the laser hits the target with 50 fs resolution. The laser-target interaction region is marked with yellow circles. (g) The measured horizontal and vertical relativistic expansion rate of the plasma ($\sim 2 \times 10^8$ m/s), and its agreement with the 3D3V particle-in-cell (PIC) simulations. For more details on the plasma expansion, see Ref. [16].

the x-ray and neutron detectors are employed outside of the chamber. Note that a few MOSFETS have been exposed to the mixed radiation environment inside the target chamber to study the radiation hardening of electronics. In the following, details of each of the detectors are outlined.

A. Electron and Ion Spectroscopy

To detect electrons and ions that are accelerated from the target, we use a magnetic spectrometer described in previous work

by our group [15]. The spectrometer makes use of two 2048-element 16-bit line CCDs positioned orthogonally inside the magnetic spectrometer to detect both ions and electrons, which are separated by magnetic deflection. The electron CCD uses a lanex screen optically glued to the sensor. The lanex is rendered light tight using a thin aluminum foil. The response of the CCD with respect to electron energy and dose has been carefully calibrated. The ion CCD uses a plastic scintillator (RC-408, Saint Gobain) coated with 50 nm of aluminum and optically glued to the sensor directly. This is calibrated via CR39 particle tracks

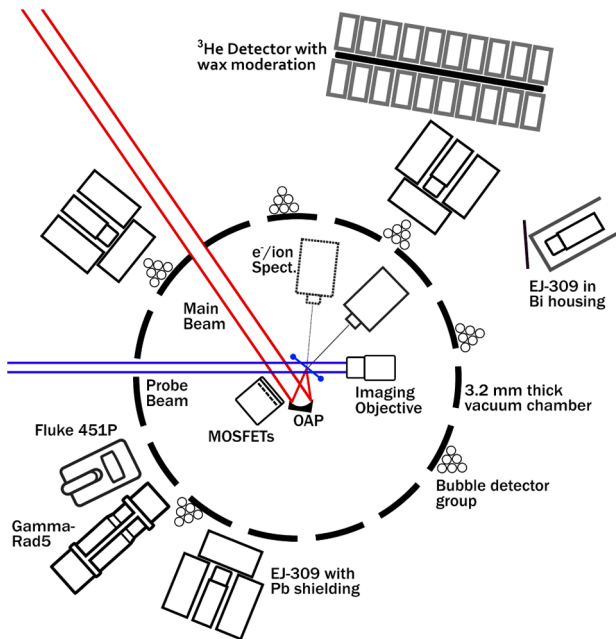


Fig. 6. A schematic highlighting the target interaction region and multiple detectors. Many of the detectors shown are designed for neutrons, including the EJ-309 liquid scintillator, bubble detectors, and the ^3He detector. A Gamma-Rad5 detector measures the x-ray spectrum in detail. A Fluke detector provides a broadband x-ray measurement. The experiment includes one electron/ion spectrometer that is shown in two different positions. A 420 nm probe beam is imaged onto a CCD in order to provide shadowgraphy of the target. The diagram includes MOSFETs near the target interaction region, which are not detectors but rather a payload that measures the effect of the radiation environment on electronics.

and also using MeV protons from a conventional accelerator. A picture of the current magnetic spectrometer is presented in Fig. 7.

When using targets such as ethylene glycol and water, one expects protons as well as carbon and oxygen ions to be accelerated from the laser-target interaction. Currently, we have no way to distinguish between these ion species. A pair of representative spectra for electrons and ions are shown in Fig. 8.

The key feature of our electron/ion spectrometer is its high repetition rate capabilities, which opened the possibility for developing ML-based control (Section 5). The spectrometer

is externally triggered by the laser and is capable of operating at repetition rates up to 100 Hz, limited by the capabilities of the line CCD. Each CCD sends its data to a virtual machine, one for the ions and one for the electrons. The virtual machines save the data in HDF5 files and also act as the EPICS server (see Section 5). These machines serve the data through EPICS to user-facing clients such as LabView, CS-Studio (Phoebus), and Python scripts used in the optimization algorithms described in Section 5.A.

B. High-Energy X-Ray Measurements

Electron acceleration naturally generates a significant x-ray environment as the relativistic electrons interact with the target and other nearby materials via bremsstrahlung and line emission. Primarily, our high-energy x-rays are generated via bremsstrahlung; as the electrons are emitted with a strong directional bias, so too are the x-rays. The x-rays produced by our facility were characterized by Morrison *et al.* [14], who found a strong backward (i.e., in the $-\vec{k}$ direction) bias to x-ray generation from a liquid water jet target. In the following, we discuss more details of the x-ray diagnostics.

For the x-ray spectrum, a Gamma-Rad5 (AmpTek) is employed, which is an integrated detector consisting of an inorganic scintillator (thallium-doped sodium iodide) and a photomultiplier tube (PMT). It is sensitive to photons between 10 keV and 3 MeV. Gamma-Rad5 is biased to 800 V and analyzed with Amptek DPPMCA software on a remote computer. The detector is placed in the target-normal rear direction in the laser polarization-propagation plane. We operate the scintillator in one of two modes: multichannel analyzer (MCA) or multichannel scaler (MCS). MCA mode allows for the collection of a time-integrated energy spectrum, while the MCS mode records the rate at which x-ray events are recorded. MCS integrates events in 10 ms intervals ($=10$ laser shots per collection) and loops indefinitely, allowing for correlation between x-ray events and other laser parameters over a long-duration experiment. Figure 9 (left) shows an example energy spectrum from our facility, as measured by Gamma-Rad5 in the MCA mode.

The Fluke 451P is a handheld ionization chamber that outputs exposure rates at 1 Hz. We position the Fluke directly outside the target chamber in the target-normal rear direction, within the laser polarization-propagation plane, and monitor the exposure rate during irradiation as a measure of the quality

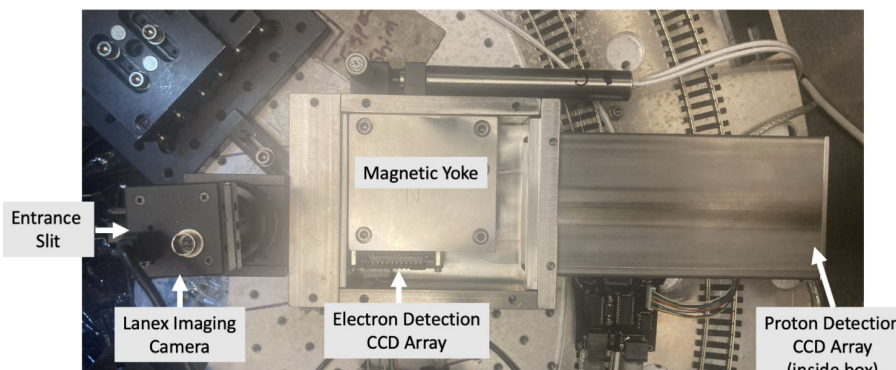


Fig. 7. Magnetic spectrometer that operates from inside the target chamber to perform electron and proton spectroscopy.

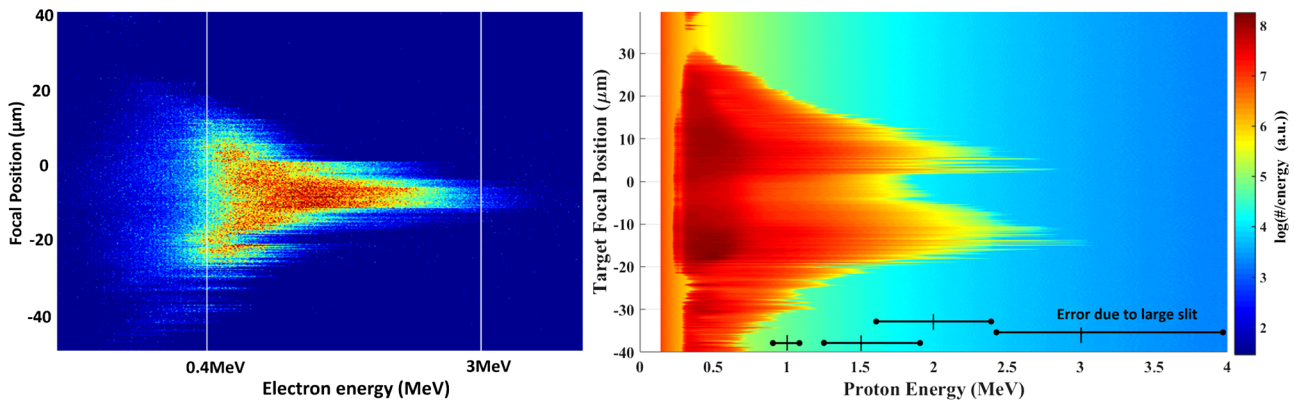


Fig. 8. Electron and proton energy spectra from tens of thousands of shots captured by the magnetic spectrometer during an optimization run for the laser focus with respect to the target. Each horizontal line spectrum represents data averaged from 10 shots, as the spectrometer linear detectors run at 100 Hz, synchronized with the kHz laser pulse train.

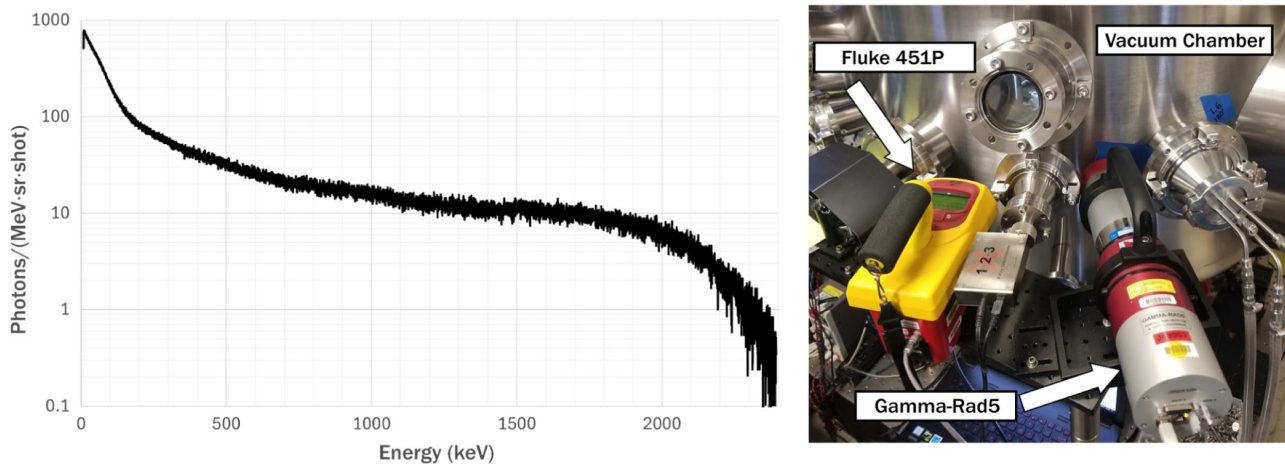


Fig. 9. (Left) Energy of emitted x-rays from extreme-intensity laser pulses on a thin liquid D₂O target as measured by the Gamma-Rad5 inorganic scintillator. Data were collected for 10 min, while the laser operated at 1 kHz. The detector subtended 0.053 ± 0.004 sr. The laser pulses contained 9.8 mJ and had no significant levels of pre-pulse. (Right) The Gamma-Rad5 inorganic scintillator and Fluke 451P ion chamber in place outside the vacuum chamber.

of our laser interactions. The x-ray exposure produced by the facility varies greatly and depends on parameters, such as pre-pulse intensity and delay, target material, and target geometry. Irradiation experiments commonly generate > 100 mR/h of x-ray exposure, and the facility is capable of producing over 1 R/h. An image of both Gamma-Rad5 and the Fluke 451P outside the vacuum chamber is shown in Fig. 9 (right).

C. Neutron Characterization

With deuterated target material, on-target intensities are large enough to generate 2.45 MeV neutrons via the $^2\text{H}(^2\text{H}, \text{n})^3\text{He}$ reaction (DD fusion). We have recently demonstrated the production of $\sim 10^5$ neutrons/s into 4π (~ 100 n/shot) and have verified their energies to be consistent with the expected 2.45 MeV [18]. Due to their neutral charge, neutrons present additional detection challenges, and so we utilize three independent detection systems to accurately characterize our neutron environment, as depicted in Fig. 6. A picture of the neutron detection suite at ELL is presented in Fig. 10. Additionally,

due to our high-flux x-ray generation, all of our detectors necessarily isolate neutron events from x-ray events, as we discuss through the remainder of this subsection.

EJ-309 (Eljen Technologies) is a liquid organic scintillator capable of detecting both neutrons and photons and discriminating between them. Each event's pulse shape determines the species of radiation via the pulse shape discrimination (PSD) technique and allows for the isolation of neutron events within the extreme x-ray environment. For further isolation of neutron events, our EJ-309 detectors are shielded by high-Z materials (Pb and/or Bi, 5 cm thick) to attenuate x-rays. We employ four separate 2.5 cm right-circular-cylindrical EJ-309 cells, each mounted to a Hamamatsu R7724 PMT, at variable locations around the experimental chamber. One EJ-309 is mounted to a 56 cm long linear actuator (Industrial Devices Corp.), allowing for remote control of that detector's position during irradiation. Each EJ-309 is connected to the same Caen DT5730S waveform digitizer and Caen DT5533EN high-voltage power supply, which biases each PMT to -1300 V. The waveform digitizer collects at a rate of 500 MSamples/s (corresponding to

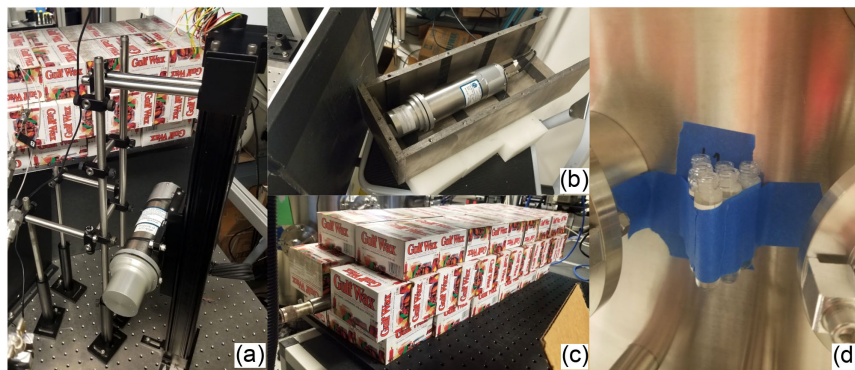


Fig. 10. Each of the neutron detectors in place around the vacuum chamber. (a) EJ-309 mounted to the linear actuator, configured to move horizontally. The midpoint of the 56 cm track is in level with the laser polarization-propagation plane. Not shown is 5 cm of lead, which surrounds the tower to attenuate x-rays. Two more stationary EJ-309s are placed at other angles and are not shown. (b) Stationary EJ-309 housed in bismuth and shielded by lead, with the top of the bismuth box removed to see inside. (c) ^3He proportional counter (metal cylinder) surrounded by wax moderation. (d) An example bubble detector group attached to the side of the vacuum chamber. Six such groups can be attached at variable points around the chamber.

2 ns between samples) and saves all samples from each event for PSD optimization in post-processing. The time of each event, as well as that of the laser trigger pulse, is also recorded via constant fraction discrimination (CFD), allowing for time-of-flight (ToF) techniques to determine the energy of each neutron event. In ToF, we use the laser trigger as a coarse approximation of the time at which neutrons were created and refine the estimate using the photon signal in the EJ-309. Additionally, the timing information of each neutron event gives the ability to correlate neutron yield with varying laser parameters; with millions of laser shots over the course of an hour-long experiment, the effect of parameters such as pre-pulse intensity and pre-pulse delay on neutron generation can be examined in a single experiment.

A ^3He proportional counter leverages the $^3\text{He}(n, ^1\text{H})^3\text{H}$ reaction: a detection of the ionization events created by the product ^1H and ^3H , which shares 762 keV, is recorded as a neutron event. Signals at other energies are discarded as electrical noise, photon events, partial capture events, or high-energy neutron scatter events. We employ an 85 cm long (active length: 76 cm), 2.5 cm diameter Reuter-Stokes ^3He proportional counter, laid horizontally just above the laser polarization-propagation plane. As the $^3\text{He}(n, ^1\text{H})^3\text{H}$ has high cross-section only for thermal neutrons ($\sigma \sim 5350 \text{ b}$), we surround our counter with paraffin wax on all sides to moderate our 2.5 MeV neutrons (6 cm thick on top and bottom, and 26.5 cm thick on front and back). The counter is biased to 1100 V and connected to NIM-standard analog electronics: an ORTEC 556 high voltage power supply, ORTEC 142PC preamplifier, ORTEC 572A linear amplifier, and ORTEC 926 analog-to-digital converter and memory (ADCAM), housed in an ORTEC 4006 NIM bin. Data are analyzed in ORTEC's Maestro multichannel analyzer software. We have previously shown that the ^3He counter is the most efficient of our neutron detectors but is also most sensitive to environmental thermalization effects, which limits knowledge of its error [18]. The absolute efficiencies of both the ^3He counter and EJ-309 detectors are determined by a GEometry ANd Tracking (Geant4) [30] Monte Carlo radiation transport simulation of the target chamber, detectors, moderation, and

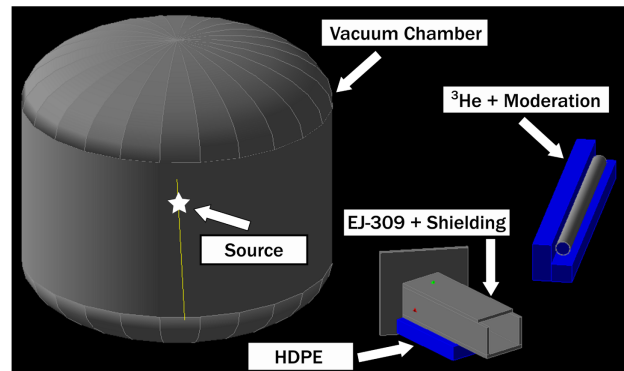


Fig. 11. Elements included in the Geant4 simulation used to estimate the absolute detection efficiency of the ^3He counter and an EJ-309. Included are the stainless steel vacuum chamber shell, high-Z shielding, and low-Z moderation of wax and high-density polyethylene (HDPE). In the simulation, neutrons are emitted isotropically from a point source at the center of the vacuum chamber.

other nearby hydrogenous materials. An image of the Geant4 model is shown in Fig. 11.

A bubble detector is a proprietary technology by Bubble Technology Industries that comprises a hydrogen-rich polymer gel and numerous “superheated” liquid droplets in a transparent, pocket-sized container. As a neutron scatters off hydrogen in the gel, the recoil proton may deposit enough energy into a droplet to push it past a phase transformation and expand into a visible bubble [31]. Other types of events do not deposit energy quickly enough to initiate the phase transformation, rendering bubble detectors gamma-blind. The bubbles are then counted after irradiation and are proportional to the neutron fluence. The detectors are then reset in a compression chamber for reuse. We employ a bubble detector spectrometer (BDS): a set of 36 such bubble detectors, in six groups of six different minimum neutron energy thresholds (10 keV, 100 keV, 600 keV, 1 MeV, 2.5 MeV, and 10 MeV). Groups of bubble detectors are placed at variable locations around the chamber, offering crude measures of angular dependence and energy unfolding. We found that bubble detectors’ gamma-blind nature renders them useful for

confirming the presence of neutrons, but their efficiency is too low, and their change in sensitivity too poorly characterized over extended use to be on par with the accuracy of our other neutron detectors [18]. An image of each of the neutron instruments is shown in Fig. 10.

5. LAB CONTROL SYSTEM AND DATA ACQUISITION: TOWARD ML-BASED OPTIMIZATION

Machine learning methods are becoming popular in RLPI fields for the optimization of various radiation outputs, like ion acceleration [32]. While detection of high-repetition-rate RLPI measurements at ELL enables high data rate acquisition to explore ML optimization, the multiple diagnostic suite requires careful synchronization of the connected computers. Many high-repetition-rate ultra-intense laser facilities are moving to a “distributed network control system” [33] model where devices are connected to a network via gigabit ethernet and data are sent in packets via network protocols [21]. The Experimental Physics and Industrial Control System (EPICS) is a framework designed to interface with devices using this distributed network control [21]. The release of EPICS v7 introduced the pvAccess network protocol framework, which is well suited for high repetition rate experiments.

Originally, our system operated with controls that exclusively used direct connection between the user interface and the device. This greatly limited the lab capabilities, so we moved to a hybrid system that uses EPICS-based and direct-connection controls. High data throughput instruments, target controls, and some laser controls were switched to EPICS. This hybrid model is an excellent example of modernizing a data acquisition and control system without fully redesigning it. The modularity of EPICS allows a lab to keep operating during this modernization process since upgrades do not usually take extensive amounts of time to implement in the lab. In this section, we summarize our implementation and highlight some

of the experimental work that it has enabled. More details about our implementation and more extensive experimental investigations are described in a recent preprint [34].

We utilize two different methods of controlling devices via EPICS. LabView is our primary method of communicating with devices via EPICS. This is done through the library CaLab [35]. Our lab uses LabView VIs to control everything in the lab, so being able to implement our EPICS devices in LabView allowed the preexisting user interfaces to remain the same, with only the back panels changing. This eased confusion with the switch to EPICS. Python is another method of communicating with EPICS-based devices, which has many user-built packages that interface between Python and EPICS. Communication via Python is mainly used in ML and optimization scripts. Figure 12 shows the integration of EPICS into some systems in the lab while others continue to use direct connection. The hybrid nature of our lab controls allows for high-throughput data acquisition and automated control of some laser and target parameters.

A. Machine Learning

The use of EPICS combined with our high-repetition-rate data-acquisition diagnostics allows for quasi-real-time optimization of the laser-plasma interaction. In the quasi-real-time optimizations, we take data from the previous 30–60 min of the experiment, combine the data using a global shot number saved with each data point, and use that to train different regression algorithms, as will be described. Before the system was fully operational, some tests were done to evaluate different algorithms using synthetic data [36,37]. These regression algorithms can currently optimize both the number of ions/electrons and the maximum energy of the ions/electrons, or any combination of those parameters. The regression algorithms use Eq. (1) as the objective function, where KE_{cutoff} is the maximum particle kinetic energy (99th percentile), $KE_{cutoff,goal}$ is the desired kinetic energy, N_e is the total number of particle

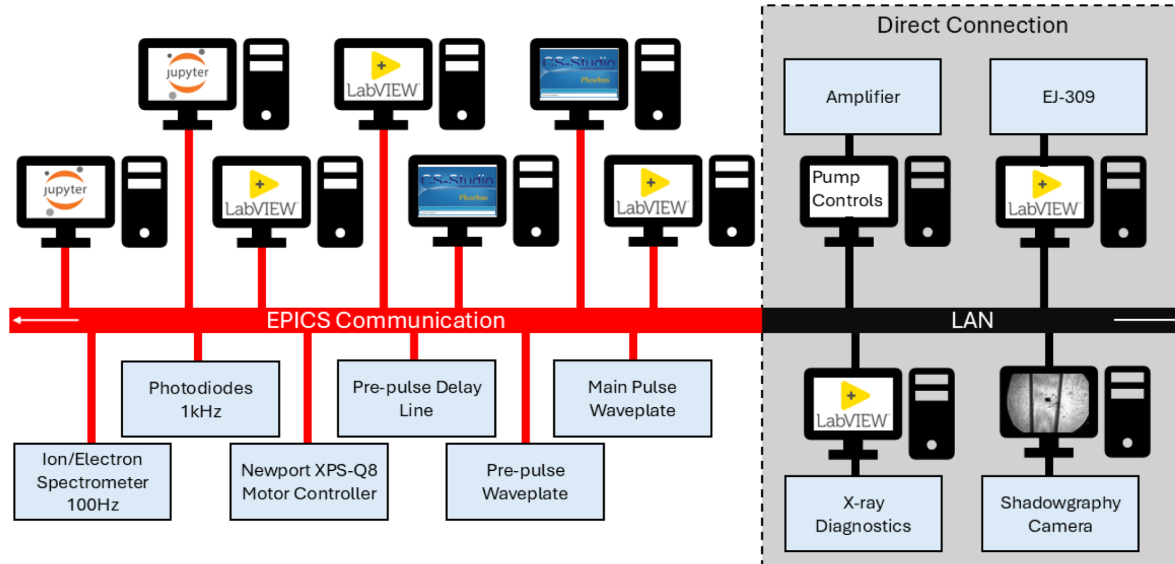


Fig. 12. Implementation of EPICS-based devices and controls working with non-EPICS devices and controls. Components in red are EPICS-based, while components in black use preexisting non-EPICS software.

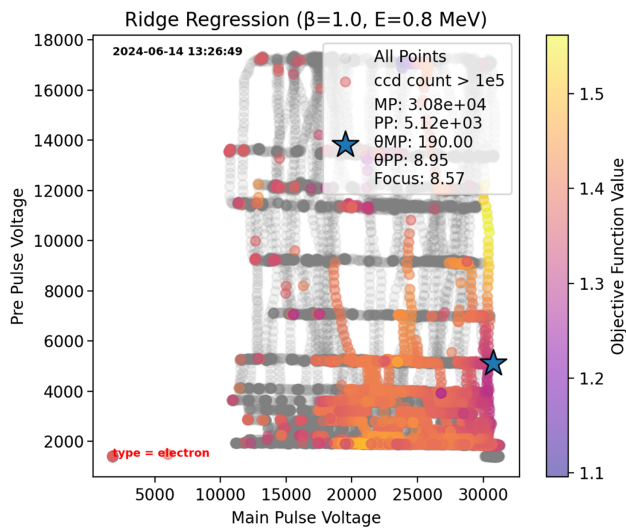


Fig. 13. In this example, the main laser pulse energy and the pre-pulse energy were varied, and the data were used to train a 6D polynomial ridge regression (discussed in Section 5.B) set to optimize for $\beta = 1$ and $KE_{\text{cutoff,goal}} = 0.8$ MeV. The pulse energies are given in diode voltages. The gray points were not used in training due to no significant electron production.

counts from the spectrometer, and β determines the relative importance between optimizing for the particle energy or the

number of particles. The factor of 8 in the denominator of the particle number term is a normalization factor that comes from each CCD pixel being represented by an unsigned 16-bit binary, and each CCD has 3648 pixels, which yields the log of the total counts of a fully saturated CCD as $\log_{10}(2^{16} \cdot 3648) = 8.38$. Figure 13 shows an example plot of minimizing the objective function:

$$f(KE_{\text{cutoff}}, N_e) = 1 + (1 - \beta) \cdot \left(1 - \frac{\log_{10}(N_e)}{8} \right) + \beta \frac{|KE_{\text{cutoff}} - KE_{\text{cutoff,goal}}|}{KE_{\text{cutoff,goal}}} \quad (1)$$

B. Regression Algorithms

Currently, three different regression algorithms are used in our optimization efforts: polynomial “ridge” regression, random forest regression, and Gaussian process regression. These algorithms are implemented using scikit-learn [38]. All hyperparameters are default from scikit-learn except for those noted. For the polynomial ridge regression model, we control the degree of the polynomial used. “Ridge” is the regularization parameter determined through cross-validation. The number of estimators (or trees) in the random forest regression is controlled by the user. All random forest regressions have a maximum depth of 10. For the Gaussian process regression, the noise level

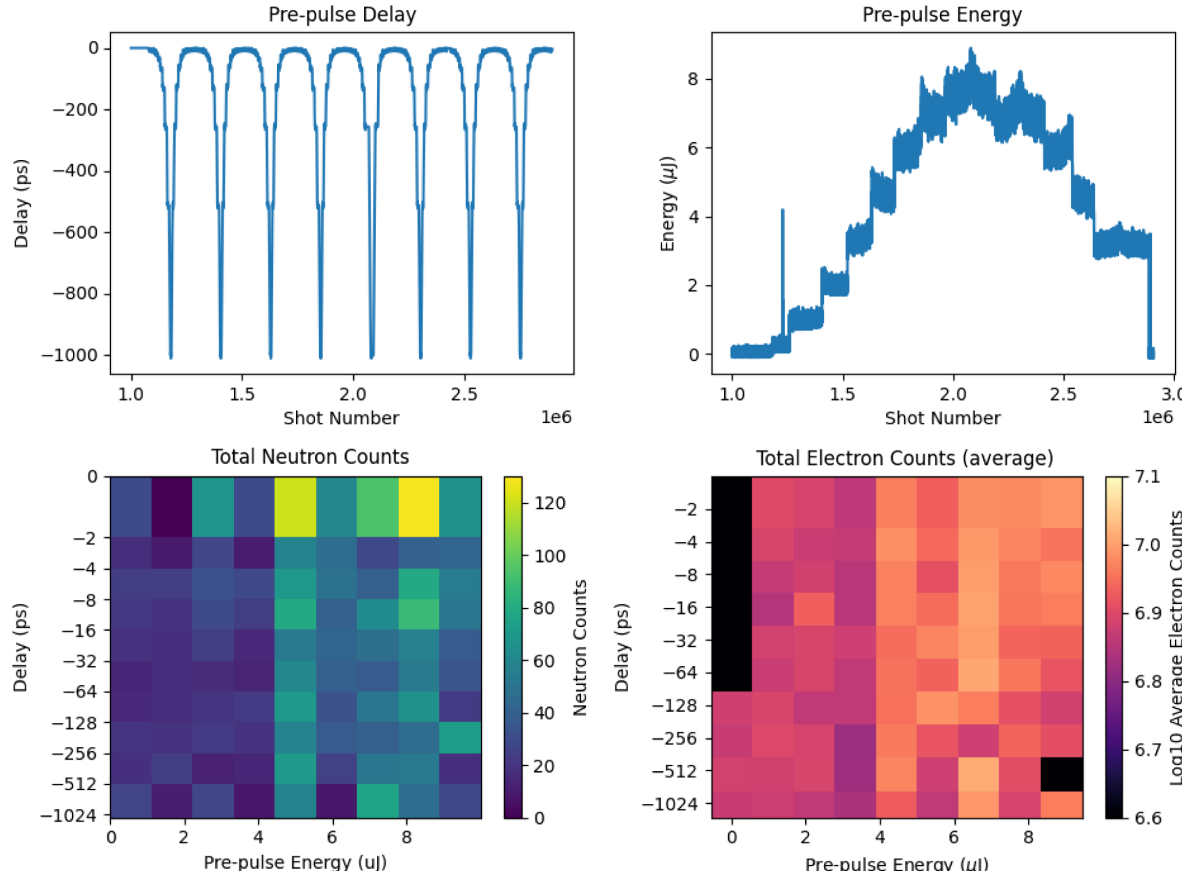


Fig. 14. Experimental data demonstrating the mixed radiation capabilities of this lab. In this experiment, the pre-pulse delay with respect to the main pulse (upper left) and pulse energy (upper right) were varied to systematically explore the parameter space. The total neutron counts (lower left) and average electron counts (lower right) were collected to search for any correlation. No optimization was done with this data.

(α) can be set by the user, which helps the regressor account for instabilities.

C. Computation and Capabilities

The suite of radiation detectors and the integration of EPICS allow the collection of mixed radiation data and laser and target parameter data at high repetition rates. Once data is collected, one can use regression algorithms to explore the parameter space and optimize different radiation outputs. Figure 14 shows an example of collecting electron and neutron data while varying laser parameters in an attempt to find the optimal parameter space for particle acceleration.

Current optimization methods are limited by the computational capabilities of our PC. In order to optimize in a quasi-real-time manner, fast training times are required. Currently, the Gaussian process regression takes the longest to train at around 1 min. The current PC used for these optimizations has an AMD Ryzen Threadripper 1900X 8-core 3.80 GHz CPU, 32 GB of RAM, and an AMD Radeon RX570 series GPU that has 8 GB of GDDR5 RAM. At present, all optimizations are done purely by the CPU.

Upgrading the PC would allow for more complex optimizations in a short enough time frame. Introducing GPU computation and upgrading the GPU would allow for more complex optimization algorithms, such as neural networks.

6. SUMMARY

The Extreme Light laboratory was established over a decade ago to explore extreme laser-driven radiations. Over the years, ELL's scientific and technical developments have grown steadily with multi-university collaborations. A brief list of accomplishments discussed here includes: (i) the development of pre-pulse control of the intense laser has allowed control of the mix of the radiation generations. (ii) Development of the liquid target has afforded us the unique kHz-rate mixed radiation generation, including kHz-rate fusion with neutron generation for at least 50 min of continuous operation. (iii) A suite of diagnostics tools are developed for electron, proton, x-ray, and neutron that can simultaneously be operated to evaluate the mixed radiation environment. (iv) The detection systems are synchronized using the EPIC server, enabling ML-based quasi-real-time control of radiation processes.

The ability to control the mix of radiations using machine learning has a wide range of applications in energy, nuclear, space, and defense enterprises, including (but not limited to): (a) building critical nuclear data, (b) parametrically understanding fusion process relevant to nuclear energy enterprise, (c) using ELL as a test platform for radiation hardening of electronics with a controllable mix of radiation mimicking an orbital environment, (d) neutron imaging for studying internal damages of critical equipments, etc.

Funding. Air Force Office of Scientific Research (23AFCOR004); Defense Threat Reduction Agency (HDTRA-1446604); National Science Foundation (2109222).

Acknowledgment. Any opinions, findings, and conclusions or recommendations expressed in this material are those of the author(s) and do not necessarily reflect the views of the federal funding agencies supporting this

research. The authors sincerely thank past members of the group, especially Dr. William "Mel" Roquemore for his vision and advocacy as founder of the ELL research program, as well as Drs. Juan Manfredi, Connor Gautam, Bryan Egner, John Morrison, Scott Feister, Kevin George, Vladimir Ovchinnikov, Steve Hageman, and Gregory Ngirmang for their numerous contributions to the development of the RLPI science and technology at ELL that are still guiding us in our current research endeavors. This work was supported by AFOSR (PM: Dr. Andrew B. Stickrath). CO and JS have been supported by the AFOSR summer faculty program. Additional support has been provided by the Defense Threat Reduction Agency and the NSF/DOE basic plasma partnership.

Disclosures. The authors declare no conflicts of interest.

Data availability. Data underlying the results presented in this paper are not publicly available at this time but may be obtained from the authors upon reasonable request.

REFERENCES

1. M. Kling, C. Menoni, and C. Geddes, "Basic research needs workshop on laser technology," Tech. rep. (US Department of Energy Office of Science, 2024).
2. A. Di Piazza, C. Müller, K. Z. Hatsagortsyan, et al., "Extremely high-intensity laser interactions with fundamental quantum systems," *Rev. Mod. Phys.* **84**, 1177–1228 (2012).
3. F. Kroll, F. E. Brack, C. Bernert, et al., "Tumour irradiation in mice with a laser-accelerated proton beam," *Nat. Phys.* **18**, 316–322 (2022).
4. W. P. Leemans, A. J. Gonsalves, H. S. Mao, et al., "Multi-Gev electron beams from capillary-discharge-guided subpetawatt laser pulses in the self-trapping regime," *Phys. Rev. Lett.* **113**, 1–5 (2014).
5. T. Ziegler, I. Göthel, S. Assenbaum, et al., "Laser-driven high-energy proton beams from cascaded acceleration regimes," *Nat. Phys.* **20**, 1211–1216 (2024).
6. W. Leemans, "Laser technology for k-BELLA and beyond," Tech. Rep. (Lawrence Berkeley National Laboratory, 2017).
7. L. Kiani, T. Zhou, S.-W. Bahk, et al., "High average power ultrafast laser technologies for driving future advanced accelerators," *J. Instrum.* **18**, T08006 (2023).
8. I. Prencipe, J. Fuchs, S. Pascaressi, et al., "Targets for high repetition rate laser facilities: needs, challenges and perspectives," *High Power Laser Sci. Eng.* **5**, e17 (2017).
9. C. Palmer, "Paving the way for a revolution in high repetition rate laser-driven ion acceleration," *New J. Phys.* **20**, 061001 (2018).
10. C. N. Danson, C. Haefner, J. Bromage, et al., "Petawatt and exawatt class lasers worldwide," *High Power Laser Sci. Eng.* **7**, e54 (2019).
11. K. M. George, J. T. Morrison, S. Feister, et al., "High-repetition-rate (> = kHz) targets and optics from liquid microjets for high-intensity laser-plasma interactions," *High Power Laser Sci. Eng.* **7**, e50 (2019).
12. S. Feister, J. A. Nees, J. T. Morrison, et al., "A novel femtosecond-gated, high-resolution, frequency-shifted shearing interferometry technique for probing pre-plasma expansion in ultra-intense laser experiments," *Rev. Sci. Instrum.* **85**, 11D602 (2014).
13. C. Orban, J. T. Morrison, E. A. Chowdhury, et al., "Backward-propagating MeV electrons in ultra-intense laser interactions: standing wave acceleration and coupling to the reflected laser pulse," *Phys. Plasmas* **22**, 023110 (2015).
14. J. T. Morrison, E. A. Chowdhury, K. D. Frische, et al., "Backward-propagating MeV electrons from 10^{18} W/cm² laser interactions with water," *Phys. Plasmas* **22**, 043101 (2015).
15. J. T. Morrison, S. Feister, K. D. Frische, et al., "MeV proton acceleration at kHz repetition rate from ultra-intense laser liquid interaction," *New J. Phys.* **20**, 022001 (2018).
16. G. K. Ngirmang, J. T. Morrison, K. M. George, et al., "Evidence of radial Weibel instability in relativistic intensity laser-plasma interactions inside a sub-micron thick liquid target," *Sci. Rep.* **10**, 9872 (2020).
17. J. Snyder, J. Morrison, S. Feister, et al., "Background pressure effects on MeV protons accelerated via relativistically intense laser-plasma interactions," *Sci. Rep.* **10**, 18245 (2020).

18. B. M. Knight, C. M. Gautam, C. R. Stoner, *et al.*, "Detailed characterization of kHz-rate laser-driven fusion at a thin liquid sheet with a neutron detection suite," *High Power Laser Sci. Eng.* **12**, e2 (2024).
19. S. M. Hooker, "Developments in laser-driven plasma accelerators," *Nat. Photonics* **7**, 775–782 (2013).
20. P. V. Heuer, S. Feister, D. B. Schaeffer, *et al.*, "Preface to special topic: the high repetition rate frontier in high-energy-density physics," *Phys. Plasmas* **29**, 110401 (2022).
21. S. Feister, K. Cassou, S. Dann, *et al.*, "Control systems and data management for high-power laser facilities," *High Power Laser Sci. Eng.* **11**, e56 (2023).
22. R. Lopez-Martens, A. Jullien, L. Canova, *et al.*, "Efficient generation of cross-polarized femtosecond pulses in cubic crystals with holographic cut orientation," *Appl. Phys. Lett.* **92**, 231102 (2008).
23. M. Noaman-Ul-Haq, H. Ahmed, T. Sokollik, *et al.*, "Statistical analysis of laser driven protons using a high-repetition-rate tape drive target system," *Phys. Rev. Accel. Beams* **20**, 1–6 (2017).
24. F. Condamine, N. Jourdain, J.-C. Hernandez, *et al.*, "High-repetition rate solid target delivery system for PW-class laser-matter interaction at ELI beamlines," *Rev. Sci. Instrum.* **92**, 063504 (2021).
25. A. Forsman, M. Do, A. Haid, *et al.*, "High repetition-rate foam targetry for laser-plasma interaction experiments: concept and preliminary results," *Rev. Sci. Instrum.* **95**, 063505 (2024).
26. B. Schmitz, D. Kreuter, O. Boine-Frankenheim, *et al.*, "Modeling of a liquid leaf target TNSA experiment using particle-in-cell simulations and deep learning," *Laser Part. Beams* **2023**, e3 (2023).
27. J. Fuchs, P. Antici, E. D'Humières, *et al.*, "Laser-driven proton scaling laws and new paths towards energy increase," *Nat. Phys.* **2**, 48–54 (2005).
28. F. Treffert, C. B. Curry, H.-G. J. Chou, *et al.*, "High-repetition-rate, multi-MeV deuteron acceleration from converging heavy water microjets at laser intensities of 10^{21}W/cm^2 ," *Appl. Phys. Lett.* **121**, 074104 (2022).
29. A. Cavagna, M. Eder, E. Chowdhury, *et al.*, "Continuous relativistic high-harmonic generation from a kHz liquid-sheet plasma mirror," *Opt. Lett.* **50**, 165–168 (2025).
30. J. Allison, K. Amako, J. Apostolakis, *et al.*, "Geant4 developments and applications," *IEEE Trans. Nucl. Sci.* **53**, 270–278 (2006).
31. B. J. Lewis, M. B. Smith, H. Ing, *et al.*, "Review of bubble detector response characteristics and results from space," *Radiat. Prot. Dosimetry* **150**, 1–21 (2011).
32. B. Loughran, M. J. V. Streeter, H. Ahmed, *et al.*, "Automated control and optimisation of laser driven ion acceleration," *High Power Laser Sci. Eng.* **11**, e35 (2023).
33. X. Ge, F. Yang, and Q.-L. Han, "Distributed networked control systems: a brief overview," *Inf. Sci.* **380**, 117–131 (2017).
34. N. Tamminga, S. Feister, K. D. Frische, *et al.*, "Towards intelligent control of MeV energy electrons and protons from kHz repetition rate ultra-intense laser plasma interactions," *arXiv*, (2025).
35. C. Wirkler, "Ca lab - labview (realtime) + epics," https://www.helmholtz-berlin.de/zentrum/organisation/it/calab/index_en.html.
36. R. Desai, T. Zhang, J. J. Felice, *et al.*, "Applying machine-learning methods to laser acceleration of protons: lessons learned from synthetic data," *Contrib. Plasma Phys.* **65**, e202400080 (2025).
37. J. J. Felice, R. Desai, N. Tamminga, *et al.*, "Applying machine learning methods to laser acceleration of protons: synthetic data for exploring the high repetition rate regime," *arXiv*, (2025).
38. F. Pedregosa, G. Varoquaux, A. Gramfort, *et al.*, "Scikit-learn: machine learning in Python," *J. Mach. Learn. Res.* **12**, 2825–2830 (2011).